JOURNAL OF GEOPHYSICAL RESEARCH, VOL. 113, D12214, doi:10.1029/2007JD009486, 2008

A Multisensor satellite-based assessment of biomass burning aerosol radiative impact over Amazonia

Falguni Patadia,[1] Pawan Gupta,[1] Sundar A. Christopher,[1] and Jeffrey S. Reid[2]

Received 10 October 2007; revised 17 January 2008; accepted 26 February 2008; published 28 June 2008.

[1] Using spatially and temporally collocated multispectral, multiangle and broadband data sets from the Terra satellite, the role of biomass burning (BB) smoke particles on cloud-free top of atmosphere (TOA) direct shortwave aerosol radiative forcing (SWARF) is examined. A 5-year analysis during the peak biomass burning months of August and September is presented over South America (0°–20°S and 45°W–65°W). Our results indicate that over 5 years, the TOA diurnally averaged SWARF (DSWARF) from the Clouds and the Earth's Radiant Energy System (CERES) scanner ranges between -5.2 Wm^{-2} and -9.4 Wm^{-2} with a mean value of -7.6 Wm^{-2} and an estimated uncertainty of ± 1.4 Wm^{-2}. The corresponding Multi Angle Spectroradiometer (MISR) aerosol optical thickness (AOT at 0.558 μm) ranged from 0.15 to 0.36 with a mean value of 0.24. The estimated mean TOA aerosol radiative forcing efficiency (E_τ) is -44.2 Wm$^{-2}\tau^{-1}$ and is in good agreement with previous studies. We also examined the beta versions of the MISR data products such as the angstrom exponent (AE) and fraction of AOT in different size bins to assess the role of BB aerosol particle properties on SWARF. Our analysis indicates that the MISR retrieved 5 year mean AE is 1.54. Contribution to total AOT from small, medium and large particles is 66%, 16% and 18% respectively. This is the first multiyear assessment of SWARF for biomass burning aerosol particles using satellite observations alone and should serve as a useful constraint for numerical modeling simulations that estimate SWARF.

Citation: Patadia, F., P. Gupta, S. A Christopher, and J. S. Reid (2008), A Multisensor satellite-based assessment of biomass burning aerosol radiative impact over Amazonia, *J. Geophys. Res.*, *113*, D12214, doi:10.1029/2007JD009486.

1. Introduction

[2] Anthropogenic biomass burning includes the burning of forests, savannas and agricultural lands for cultivation purposes, usually for accommodating the needs of the expanding population. It releases trace gases such as carbon dioxide and ozone, releases more than 100 Tg of aerosol particles annually in the tropics [*Hao and Liu*, 1994] and has the potential to significantly alter regional to global climate [*Kaufman et al.*, 2002]. While most of the biomass burning (BB) activities occur in Africa, South America is responsible for emitting about 30 Tg of aerosols annually [*Andreae*, 1991]. On a regional scale, in the Southern hemisphere dry season that peaks during August–September, the biomass burning smoke in South America can cover nearly 4–5 million km^2 [*Prins et al.*, 1998] and can affect the regional radiation balance significantly [*Christopher et al.*, 2000] by scattering and absorbing solar radiation. Since biomass burning has a strong annual cycle that peaks during the dry season of a given geographic region, the resultant aerosol radiative forcing is also inhomogeneous and therefore is a large source of uncertainty in regional climate projections. Robust observational constraints on the response of a climate model [*Stott and Kettleborough*, 2002; *Stott et al.*, 2006] to aerosol forcing can aid in reducing these regional uncertainties. Hence it is imperative to assess the radiative impacts of biomass burning aerosol particles at regional scales using large number of near simultaneous measurements over large spatial and temporal domains.

[3] Since the launch of the Terra satellite in 1999, a new generation of satellite sensors such as the Moderate Resolution Imaging SpectroRadiometer (MODIS) and the Multi-Angle Spectroradiometer (MISR) have offered superior capabilities for detecting fires [*Giglio et al.*, 2003], and retrieving aerosol particle properties such as aerosol optical thickness (AOT) and particle sizes globally [e.g., *Remer et al.*, 2005; *Kahn et al.*, 2005]. The radiative effect of aerosol particles at the top of atmosphere (TOA) can be calculated using aerosol particle properties from these observations and coincident broadband flux from radiative transfer (RT) calculations [*Procopio et al.*, 2004] or from data sets such as the Clouds and the Earth's Radiant Energy System (CERES) [*Christopher and Zhang*, 2004].

[4] In this paper we use multisensor (MODIS, MISR, CERES on Terra) satellite observations to estimate the TOA

[1]Department of Atmospheric Science, The University of Alabama in Huntsville, Huntsville, Alabama, USA.
[2]Aerosol and Radiation Section, Marine Meteorology Division, Naval Research Laboratory, Monterey, California, USA.

0148-0227/08/2007JD009486

shortwave aerosol radiative forcing (SWARF) over South America for 5 years. This approach does not require the more involved RT calculations [*Procopio et al.*, 2004] and has been used earlier to calculate TOA SWARF over global oceans [e.g., *Zhang et al.*, 2005; *Christopher et al.*, 2006] and to assess the effect of aerosol particles on regional radiative fluxes using the MODIS/MISR/CERES [*Zhang and Christopher*, 2003]. However, to our knowledge there are no studies that have quantified the effect of biomass burning aerosol particles over South America using multiyear MODIS, MISR and CERES data. The only multiyear observational study that reported SWARF over South America was by *Procopio et al.* [2004] who used AERONET aerosol particle properties from two locations and calculated the SWARF at the TOA and at the surface using Discrete Ordinate Radiative Transfer (DISORT). They also conclude in their study that results from point locations cannot be extrapolated to regional scales since aerosol particle properties, the atmosphere and the surface properties change as a function of space and time. This necessitates the use of multisensor satellite data to calculate SWARF from regional to global scales.

[5] The goal of this study is two fold. The first goal is to provide a multiyear assessment of TOA SWARF over a region dominated by biomass burning in South America and to quantify the SWARF as a function of AOT which is usually called aerosol forcing efficiency (E_τ) that is a useful parameter for comparison with modeling studies. To accomplish this task, we collocate 5 years (2000–2005) of MISR and CERES data in space and time for the months of August and September when BB activities in South America are at its peak. The CERES data used in this study already contains coregistered MODIS data. MODIS AOT within CERES footprint is denoted by τ_{MODC} in the paper. Comparison of MODIS and MISR AOT with AERONET show that over land, MISR AOT compares well with AERONET than MODIS AOT [*Abdou et al.*, 2005; *Kahn et al.*, 2005]. However, 36 spectral channels of MODIS facilitate good cloud clearing capabilities. Thus we use the coregistered MODIS cloud-cover information to identify clear sky CERES TOA shortwave fluxes (SWF) by eliminating cloud-contaminated pixels and we use the collocated MISR AOT (τ_{MISRC}) to identify CERES pixels containing aerosol particles [*Gupta et al.*, 2008]. The TOA SWARF is then calculated by differencing the TOA clear and aerosol sky fluxes. The collocated MISR AOT (τ_{MISRC}) is then used to examine the relationship between AOT and SWARF to derive E_τ.

[6] The second goal which is purely exploratory is to use aerosol data products from the MISR that are not yet fully validated such as the angstrom exponent (AE) and fractionated AOTs in three particle size bins, small (<0.35 μm) (SAOT), medium (0.35–0.7 μm) (MAOT), and large (>0.7 μm) (LAOT) to examine the use of such observations in analyzing the radiative effects of aerosol particles. Though comprehensive AOT validations with the AERONET have been accomplished by the MODIS and MISR science teams [*Remer et al.*, 2005; *Kahn et al.*, 2005; *Abdou et al.*, 2005] we compare the merged MISR aerosol particle properties within CERES footprint from this study against space and time collocated AERONET data.

2. Data and Study Area

[7] We analyzed 5 years (2000–2005) of data during the peak biomass burning season (August–September) in South America. Figure 1 shows the study area between 0°–20°S and 45°W–65°W. All available AERONET stations in this area and during the study period are shown in black symbols. A brief description of the sensors and the data sets used in this study are given here for completeness since details are available elsewhere in the literature for MODIS aerosol [*Remer et al.*, 2005], MODIS fire [*Giglio et al.*, 2003], MISR aerosol [*Kahn et al.*, 2005], CERES SSF [*Wielicki et al.*, 1996] and AERONET aerosol products [*Holben et al.*, 2001].

2.1. MODIS Aerosol and Fire Product

[8] The MODIS measures reflected and emitted radiation from the earth-atmosphere system in 36 spectral channels between 0.405 μm–14.385 μm, with a swath width of 2330 km and near daily global coverage. While the original measurements are at 250 m, 500 m and 1 km, the level 2 (L2) aerosol product (MOD04_L2 collection 4) is available at 10 km^2 that is generated from 20 × 20 pixel box or 400 pixels at 500 m resolution. The land algorithm uses reflectance from 3 channels (0.47, 0.66, 2.13 μm) with a reported uncertainty in AOT of ±0.05 ± 0.15 * AOT0.55 [*Remer et al.*, 2005]. The MODIS AOT (τ_{MODC}) and MODIS cloud cover information in CERES SSF data product have been used in this study. Although the new MODIS L2 collection 5 data product is now available [*Levy et al.*, 2007] the CERES SSF product that is used for this study has not yet been processed at the Langley DAAC to include this data and only contains MODIS data from collection 4.

[9] MODIS measurements are also used for fire detection using a contextual algorithm [*Giglio et al.*, 2003] based on strong emission of mid-IR radiation from fires. Each MODIS pixel is examined and categorized into cloud, water, nonfire, fire, unknown or missing data. In this study we use the Climate Modeling Grid fire product from MODIS (MOD14CMH) [*Justice et al.*, 2002; *Morisette et al.*, 2005] to analyze fire activity in the study region and to see if it corroborates with trends in AOT as the MODIS fire data are also based on observations from the same satellite overpass time. This product contains monthly gridded (0.5° × 0.5°) statistical summaries of fire pixels.

2.2. MISR Aerosol Product

[10] The MISR has four spectral bands (0.446 μm, 0.558 μm, 0.672 μm and 0.866 μm) and nine cameras with a swath width of 360 km that requires about 9 d for global coverage. Coregistered multiangle and multispectral MISR data at 1.1 km^2 are used for aerosol retrievals in MISR Level 2 aerosol product (MIL2ASAE) which is used in this study to identify aerosol particles within CERES pixels. The L2 retrieval is performed over a 17.6 km^2 region which contains 16 × 16 pixels of 1.1 km^2 resolution. Homogeneity of atmospheric aerosol particles is assumed within each region. Two distinct algorithms are used for aerosol retrievals over dark water and heterogeneous land. For aerosol retrievals over land, information from all 36 channels (9 cameras and 4 channels) is required Similar to the MODIS, a lookup table (LUT) approach is used for aerosol retrieval. From mixtures of different aerosol

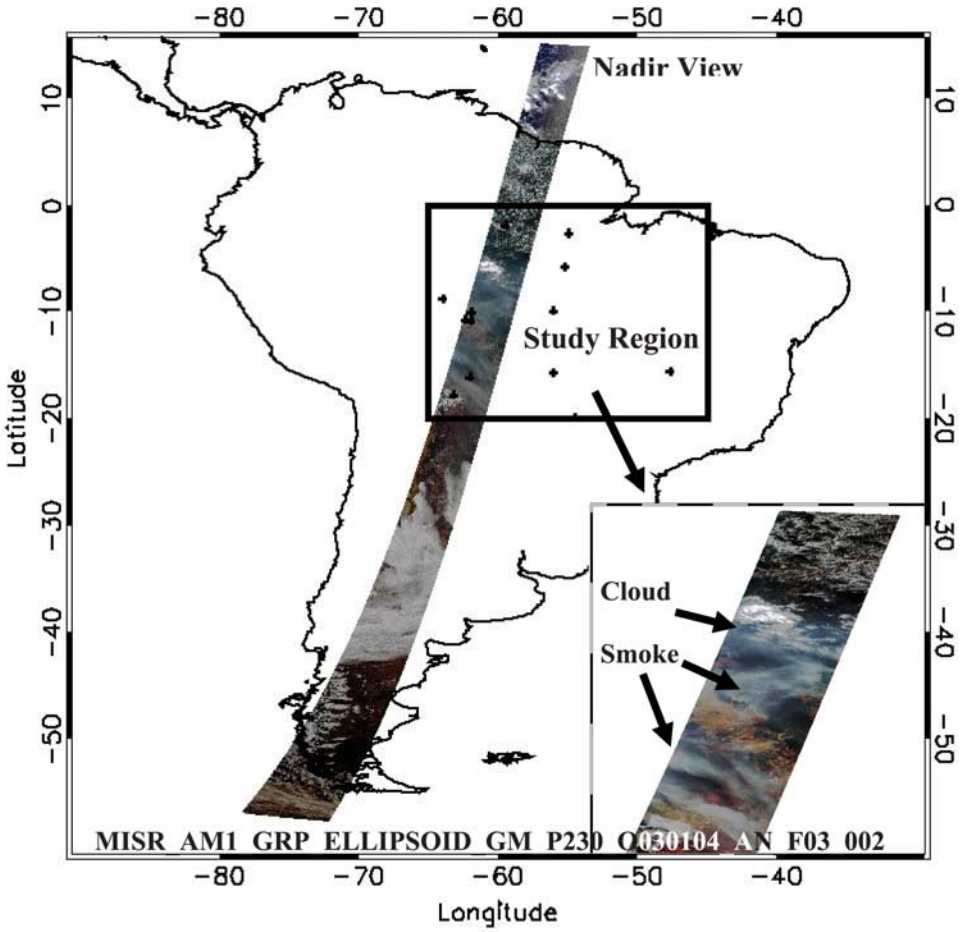

Figure 1. Study area enclosing 0°–20°S and 45°W–65°W. All available AERONET stations in this area and during the study period are shown in black symbols. An MISR image from nadir viewing camera (filename indicated at bottom of figure) for 15 August 2005 is overlaid on the map and the inset shows smoke event over the study region (see labels).

components, 74 aerosol models are defined. The mixtures are defined in the mixture file and the aerosol components are described in aerosol physical and optical properties (APOP) file. Region averaged MISR radiances are compared to the simulated TOA equivalent reflectances. Aerosol properties (e.g., total AOT, SAOT, MAOT, LAOT, SSA, AE) from all models that satisfy a given set of χ^2 acceptance criteria are reported as successful retrievals. A detailed description of the MISR aerosol retrieval is given by *Martonchik et al.* [1998, 2002].

[11] When compared to AERONET data, the MISR retrieved AOT (τ_{MISRL2}) is within the maximum of ±0.05 or ±0.2 * AOT0.558 over both land and water [*Kahn et al.*, 2005]. A recent study by *Abdou et al.* [2005] reported that over the global land areas, the MISR aerosol retrievals compare well with AERONET when compared with MODIS retrievals against AERONET, which is one of the reasons for using the MISR retrievals in this study. We use versions 15 to 19 of MIL2ASAE and the highest version of available MIL2ASAE data was used for each year. The unavailability of the same version of data set in all years results in the choice of different versions of MIL2ASAE data used. The AOT difference between higher and lower versions of the MISR product for the area of study was found to be of the order of 0.01. Since this value is within the maximum uncertainty in τ_{MISRL2} (±0.05) we consider its impact on forcing to be within the estimated uncertainties. The MISR aerosol data product also contains unique information on aerosol properties such as AE, SAOT, MAOT, and LAOT. Though these products are deemed "unvalidated" we use these products in an exploratory mode for qualitative analysis of SWARF as a function of these properties and to examine them against known values in the literature.

2.3. AERONET Data

[12] AERONET is a federation of well calibrated ground based Sun photometers [*Holben et al.*, 1998]. These instruments provide global observations of AOT at seven wavelengths along with other inversion products [*Holben et al.*, 2001; *Dubovik and King*, 2000]. The estimated uncertainty in AERONET AOT is about ±0.015 [*Holben et al.*, 2001]. We use Version-2 Level-2 hourly AOT and AE data for all 5 years of study from 13 stations in our study area (Figure 1) to evaluate the MISR AE, and τ_{MISRC}. The CERES-MODIS-MISR data set from this study was collocated in space and time with available AERONET stations within the study area. Mean of data from MISR within

±0.25° (or 3 × 3 CERES pixels) around the AERONET site was calculated. Arithmetic average of AERONET observations within ±30 min of CERES observation was then reported to compare against satellite observations. The mean AERONET AOT is denoted by τ_{AEROC} in the paper.

2.4. CERES-SSF Product

[13] The CERES instrument onboard Terra satellite makes broadband radiance measurements [*Wielicki et al.*, 1996] at the TOA, both in the longwave (LW) and shortwave (SW) parts of the electromagnetic spectrum. The CERES instrument has three channels: a SW channel for measuring reflected sunlight (0.3–5 μm), an infrared (IR) channel (8–12 μm) for measuring Earth-emitted thermal radiation "window" region, and a total channel (0.3–200 μm) for total radiation measurement. The well-calibrated radiance measurements are then converted to reflected and emitted fluxes using angular dependence models [*Loeb et al.*, 2003a, 2005]. The Terra satellite carries two identical CERES instruments including Flight Model 1 (FM1) operating in the cross-scan mode and Flight Model (FM2) in a biaxial scan mode. Measurements from biaxial scan mode are used for developing angular models to convert the measured broadband radiances to fluxes which is a considerable improvement over previous generation of instruments such as the ERBE [*Loeb et al.*, 2003b, 2007]. In this study we use the Single Scanner Footprint TOA/Surface Fluxes and Clouds (SSF) product (http://asd-www.larc.nasa.gov/DPC/DPC.html) which contains 1 h of instantaneous CERES data for a single scanner and merged information from higher-resolution MODIS imager on Terra (CER_SSF_Terra-FM1-MODIS_Edition2B-Rev1). In this product, the higher-resolution MODIS data such as AOT (τ_{MODC}), scene identification and cloud and aerosol properties are averaged over the larger CERES footprint using point spread functions [*Smith*, 1994]. TOA SW fluxes, τ_{MODC} and MODIS cloud cover [*Martins et al.*, 2002; *Minnis et al.*, 2003] information are used from the SSF product along with other data quality flags.

3. Methodology

[14] To collocate MISR data with CERES SSF data all MISR pixels falling within this CERES footprint corresponding to the same time are located and the arithmetic average of parameters of interest is computed [*Gupta et al.*, 2008]. No point spread function (PSF) weighting is assigned but the uncertainties due to that may be small since the spatial resolution of MISR aerosol product at nadir (17.6 km^2) is close to that of CERES footprint at nadir (20 km^2) and the narrow swath width of MISR limits the change of respective pixel sizes away from nadir. However, the change in CERES footprint size is accounted for in the collocation algorithm [*Gupta et al.*, 2008]. Once the data sets are collocated, the mean and standard deviations of τ_{MODC}, τ_{MISRC}, the fractionated optical depths, AE and the CERES SSF data are stored for further analysis. All analysis is done using this merged MODIS, MISR and CERES data set.

[15] Estimation of SWARF requires cloud free CERES shortwave flux measurements. Using the MODIS cloud cover information (retained in the merged data set from the CERES SSF product) cloudy pixels are first removed if cloud fraction is > 0.5% and for subpixel clear area percentages > 99.9%. Also, our analysis is restricted to CERES pixels with viewing and solar zenith angles less than 60° to avoid using large pixel sizes at large scan angles. We use clear sky data by choosing cloud free CERES pixels but subpixel cloud contamination poses a potential uncertainty in the analysis. This uncertainty is obtained by relaxing the percentage cloud cover by 1%, 5% and 10% and calculating the resulting forcing. This changes diurnal average SWARF by ~0.5 Wm^{-2}.

[16] Data from 2004 were eliminated in subsequent analysis because 97% of the data was rejected based on cloud clearing criteria and more than 90% of the remaining data had AOT values smaller than 0.2 resulting in AOT-SWARF relationships that are not statistically representative. In other years, on an average, more than 25% data was usable after cloud clearing and by applying other quality checks. Investigation of AERONET measurements during August–September of 2004 also show many missing observations over most of the stations in the study area (Figure 1) and during the satellite overpass time. The cloud cover, fire count, water vapor content and temperature distribution over the study region for all the years was intercompared to explore the reason for missing data in 2004. The variations in these fields did not show discrepancies that could explain the unavailability of data in 2004 under clear sky conditions and the reason for this is unclear. We speculate that thick smoke from fire events might have been misidentified as clouds leading to exclusion of data in our study.

[17] In cloud-free sky conditions, the shortwave aerosol radiative forcing (SWARF) is defined as the difference in TOA shortwave fluxes from the CERES in the absence (F_{clr}) and in the presence (F_{aero}) of aerosols (SWARF = $F_{clr} - F_{aero}$). To calculate TOA instantaneous SWARF during the time of the satellite overpass, two values are needed. The first is the clear sky (cloud and aerosol particle free) shortwave flux (i.e., F_{clr}) and the second is the cloud free shortwave flux due to BB aerosol particles (i.e., F_{aero}). It is not possible to obtain F_{clr} and F_{aero} for the same pixel during the satellite overpass and therefore approximations are needed to calculate F_{clr}. Previous approaches have used the lowest SWF over a time period to obtain F_{clr} [*Christopher and Zhang*, 2002] while others have used RT calculations to obtain F_{clr} for zero AOT conditions. In this study, a regression relationship between all τ_{MISRC} and TOA CERES SWF for each 0.5° × 0.5° latitude-longitude grid is formed and the y-intercept of the regression line is reported as the F_{clr} for zero AOT conditions similar to methods outlined by *Zhang et al.* [2005]. However, note that by *Zhang et al.* [2005] the LUT for F_{clr} was computed for 2° × 2° grid as a function of wind speed, solar zenith angle and for AOT < 0.2 and they applied this technique to near-uniform dark ocean background whereas we apply this regression technique to the Amazon and savanna regions over South America. The assumption in our method is that over the study period, the surface albedo is quasi-uniform in 0.5° × 0.5° grids and F_{clr} is computed only if number of data points within a grid is >10 and positive correlation exists (r > 0.2) between SWF and τ_{MISRC}. Since F_{clr} has been calculated by regressing SWF

Table 1. Comparison of Area-Averaged Seasonal (August–September) MODIS and MISR Aerosol Properties in CERES Footprint for 2001–2005 for the Region of Study (0°–20°S and 45°W–65°W)[a]

Year	Data Points	τ_{MODC}	τ_{MISRL2}	τ_{MISRC}	AE	% SAOT	% MAOT	% LAOT
2000	7754	0.19 ± 0.18	0.23 ± 0.18	0.18 ± 0.14	1.47 ± 0.30	72	6	22
2001	21430	0.15 ± 0.15	0.22 ± 0.18	0.15 ± 0.12	1.41 ± 0.31	73	7	20
2002	19146	0.35 ± 0.35	0.39 ± 0.31	0.30 ± 0.24	1.58 ± 0.36	77	10	13
2003	18814	0.25 ± 0.25	0.30 ± 0.26	0.23 ± 0.18	1.89 ± 0.47	43	44	13
2004[b]	*1777*	*0.19 ± 0.30*	*0.35 ± 0.33*	*0.15 ± 0.16*	*1.85 ± 0.42*	*19*	*75*	*6*
2005	33907	0.43 ± 0.42	0.40 ± 0.32	0.36 ± 0.28	1.35 ± 0.30	67	14	19
Mean	20210	0.27 ± 0.12	0.31 ± 0.09	0.24 ± 0.09	1.54 ± 0.22	66	16	18

[a]Also listed are the associated standard deviations. τ stands for aerosol optical thickness and its subscript MOD stands for MODIS, MISRL2 for MISR L2 AOT and MISRC for MISR AOT within the CERES footprint. AE denotes the angstrom exponent from MISR. The percentage contribution of Small (%SAOT), Medium (%MAOT) and Large (%LAOT) mode aerosols to the total AOT (τ_{MISRC}) is also tabulated. The second column shows the number of valid collocated data points used in calculating statistics of merged data. The number of data points used to calculate τ_{MODC} and τ_{MISRL2} statistics are different (higher).

[b]2004 is shown in this table only for the sake of completeness and the corresponding values are not considered representative. This year has not been included in analysis for reasons cited in text. Table shows mean of years 2000, 2001, 2002, 2003, 2005 only.

against MISR AOT (Figure 4) any uncertainty in MISR AOT and SWF must translate to an uncertainty in F_{clr}. Assuming that these uncertainties are not correlated they are estimated separately. The uncertainty in F_{clr} due to AOT is estimated using the following relationship.

[18] F_{clr} Uncertainty (Wm^{-2}) = $E\tau$ ($Wm^{-2}\tau^{-1}$) × Maximum uncertainty in MISR AOTwhere $E\tau$ is the TOA instantaneous aerosol radiative forcing efficiency defined as the derivative of instantaneous SWARF as a function of AOT ($Wm^{-2}\tau^{-1}$) [*Li et al.*, 2004; *Jones and Christopher*, 2007]. An uncertainty of 2.2 Wm^{-2} (or ±1.1 Wm^{-2}) in clear sky flux (F_{clr}) is estimated using maximum uncertainty in MISR AOT of ±0.05 and mean $E\tau$ of −44.2 $Wm^{-2}\tau^{-1}$. The uncertainties in SWF are due to the unfiltering of SW radiances and the radiance to flux conversion using ADMs and are cited in literature [*Loeb and Kato*, 2002]. We use these values from literature (see Table 5) and the results and discussion section presents a comprehensive assessment of all the uncertainties.

[19] Aerosol sky fluxes are obtained from CERES pixels that have a valid τ_{MISRC} value but with no clouds as reported by the MODIS. However, stringent cloud clearing criteria used in this study results in SWARF that is biased toward CERES cloud free skies and therefore requires sample bias (B) adjustments [*Zhang et al.*, 2005]. Collocation of τ_{MISRL2} within CERES footprint also results in slightly lower AOTs (i.e., τ_{MISRLC}) compared to τ_{MISRL2} (Table 1) because of small differences in the CERES and MISR spatial resolutions. The estimated instantaneous SWARF has been corrected for the sample bias from cloud free skies using the following formula:

$$\text{Bias Corrected Instantaneous SWARF} = (E\tau * B) + \text{Instantaneous SWARF}$$

where B is the sample bias and is the difference between the τ_{MISRL2} and cloud free τ_{MISRC}. The bias was determined for each year and gridded separately and the instantaneous SWARF was corrected for sample biases. After bias correction, diurnal average of SWARF (DSWARF) was performed using methods outlined by *Remer and Kaufman* [2005].

[20] In this study we qualitatively analyze the type of aerosol particles that dominate during BB activities by assessing the AE, SAOT, MAOT, and LAOT values from MISR. Since these are beta quality products we first compared them with spatiotemporally collocated AERONET observations. For this, the mean of cloud free valid MISR parameters (from merged product) in 3 × 3 pixels around the AERONET site is calculated. All valid AERONET data within ±30 min of satellite observations are also averaged. The merged MISR SAOT, MAOT, and LAOT information are also used for the first time in this study to gain some insight of sizes of aerosol particles associated with biomass burning activities and to examine their trends and interrelationship with DSWARF. In the remainder of the paper, the bias corrected TOA instantaneous SWARF will be simply referred to as SWARF, diurnally averaged SWARF as DSWARF and 5 year (2000–2005, minus 2004) seasonal (August–September) mean values as the mean.

4. Results and Discussion

[21] Multiyear analysis of satellite data in this study shows an increasing trend in the seasonal mean AOT over the study region from the year 2000 to 2005 (Table 1). Since AOT is proportional to the concentration of smoke particles, an increase in AOT must relate to increased biomass burning activities in the region. To support this argument, the MODIS fire count data (MOD14CMH) was acquired and the total fire count in the study region was computed for each year. Figure 2 shows a good correspondence between the τ_{MISRC} and fire count from MODIS. Increase in both AOT and fire count indicates that the fire activities in the study region have increased from 2000 to 2005. Increasing biomass burning activity necessitates the evaluation of the impacts (SWARF in our case) of biomass burning aerosol particles. Note that there was a reduction in biomass burning of more than 40% in 2006 due to a tri-national policy shift implemented in 2006, according to a recent paper by *Koren et al.* [2007]. However, they also observe a sustained increasing trend in AOT and fire data during 2000–2005.

[22] The estimation of forcing in this study is presented below and the results are organized such that the two goals of this study are addressed one after the other. SWARF estimation (first goal) uses the merged τ_{MISRC} and CERES SW fluxes. The collocation of MISR L2 AOT (τ_{MISRL2}) within CERES footprint (τ_{MISRC}) is first evaluated followed by a summary of estimates of F_{clr}, F_{aero}, SWARF, AE, and AOTs. The relationship between estimated SWARF and

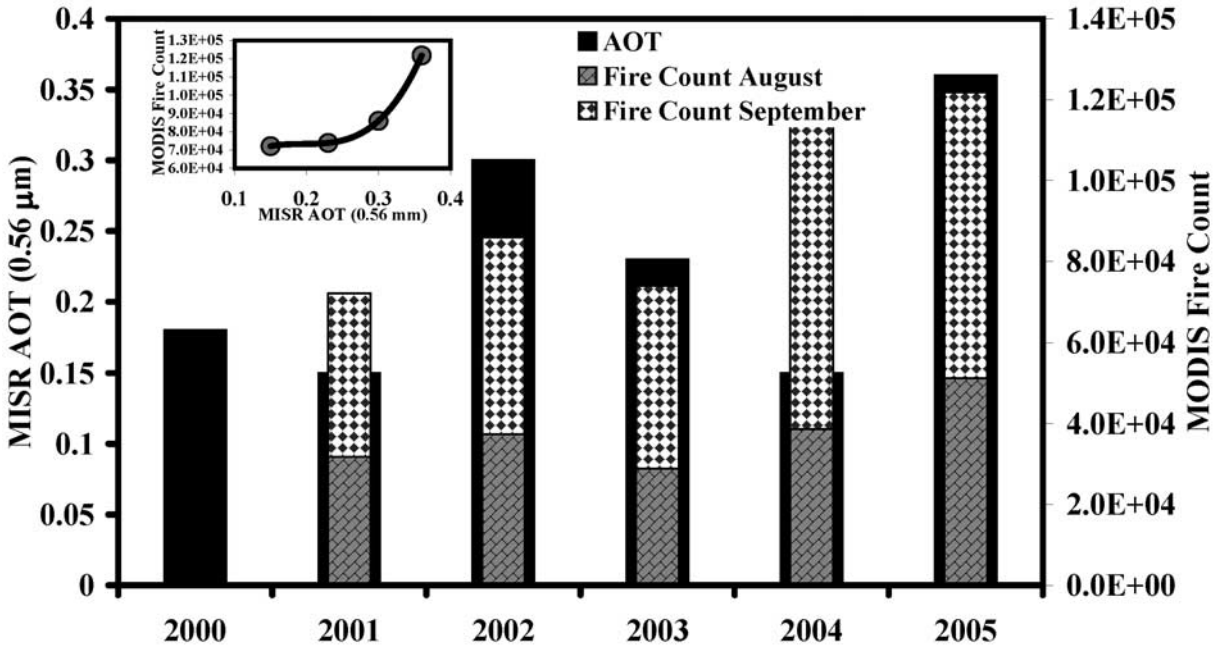

Figure 2. Histogram of seasonal area-averaged MISR AOT (AOT) within CERES footprint and MODIS fire product based total fire count (Fire Count) in the study region for 2000–2005. The fire count data for the year 2000 was not available. Fire count for August and September are shown separately for each year. Inset shows the variation of MODIS fire count with MISR AOT.

τ_{MISRC} which is used to infer E_τ is then discussed. We then present the qualitative analysis of interrelationship of DSWARF and merged MISR beta products (second goal). For completeness, the MISR AE, SAOT, MAOT, LAOT are first compared to available AERONET observations. Results and discussions on the daily variation of DSWARF, τ_{MISRC}, SAOT, MAOT, and LAOT is then presented followed by the interannual variation in all parameters and their interrelationships. Finally an uncertainty analysis of estimated SWARF is presented.

4.1. Collocation of MISR AOT Within CERES Footprint

[23] To calculate SWARF from our collocated data set, we first assess our collocation by examining the relationship between the τ_{MODC}, τ_{MISRC}, and τ_{AEROC} within each CERES footprint over the entire period of study. Figure 3 shows the comparison of these AOTs. The insets show the frequency distribution of τ_{MODC} and τ_{MISRC}. The gray dots in Figure 3 depict relation between τ_{MODC} and τ_{MISRC} at CERES pixel resolution from all 5 years. For each year, the mean τ_{MODC} in eleven τ_{MISRC} bins was calculated and is shown in different black symbols in Figure 3. In AOT bins with τ_{MISRC} values <0.3 there is a very good agreement between τ_{MODC} and τ_{MISRC} with τ_{MISRC} being higher than τ_{MODC} by 0.01. In bins with $\tau_{MISRC} \geq 0.3$, the τ_{MODC} is higher than τ_{MISRC} by 0.12. Closer examination of AOT differences in the eleven τ_{MISRC} bins shows that the differences increase with increase in AOT and become nonlinear at higher AOT (>0.3) values. The area averaged seasonal mean values of τ_{MODC} and τ_{MISRC} for each year are also in better agreement when AOT < 0.3 (see year 2000, 2001, 2003, and 2005 in Table 1). During the multi year (minus 2004) study period, within the CERES footprint, the mean τ_{MISRC} was 0.24 while mean τ_{MODC} was 0.27 (Table 1) and the mean τ_{MODC} exceeds τ_{MISRC} by about 16%. These results are consistent with the study by *Abdou et al.* [2005] which shows that over land, MODIS retrieved AOTs at 470 and 660 nm are 35% and 10% larger than those retrieved by MISR for all land surface types. However, these relationships may be different with the newer versions of the MISR and MODIS products. Figure 3 also shows τ_{AEROC} from all 5 years as a function of both τ_{MISRC} and τ_{MODC} in different symbols. A total of 45 data points from 13 AERONET stations were collocated with τ_{MODC} and τ_{MISRC}. Table 2 lists the mean and standard deviation of the space and time collocated τ_{AEROC}, τ_{MISRC}, and τ_{MODC}. Agreement between τ_{AEROC} and τ_{MISRC} is good for AOT< 0.5 (see years 2000, 2001, and 2003 in Table 2). For higher AOT values (>0.5) τ_{MISRC} is less than τ_{AEROC} (see 2002, 2005 in Table 2). *Kahn et al.* [2005] also found MISR midvisible AOT values to be lower than AERONET during peak of southern biomass burning season and attribute it to the more absorbing mixtures of spherical particles picked by retrieval algorithm in biomass burning season. The 5-year mean correlation between τ_{MODC} and τ_{MISRC} of 0.94 and correlation of 0.96 between τ_{AEROC} and τ_{MISRC} strengthens the confidence in the MISR collocation performed for this study and its use in forcing estimation.

4.2. TOA Shortwave Aerosol Radiative Forcing

[24] Table 3 summarizes the values of τ_{MISRC} and the corresponding shortwave fluxes (F_{clr} and F_{aero}), instantaneous, bias adjusted and diurnally averaged SWARF and $E\tau$ for the 5 years of study. F_{clr} was computed from regression relationship between τ_{MISRC} and F_{aero} in every 0.5 × 0.5 latitude-longitude grids. Over the 5 years, a mean of 12 to 33 data points were used for calculating F_{clr} within

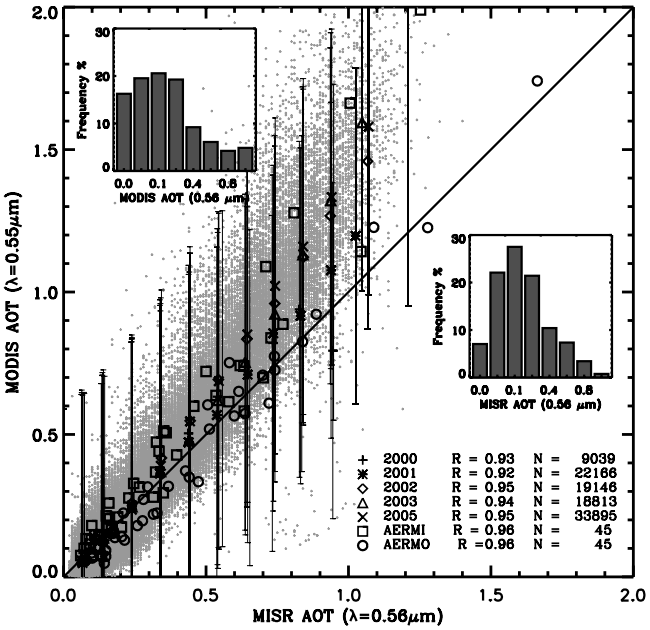

Figure 3. Relationship between MODIS and MISR AOT collocated within the CERES footprint for 2000–2005 (August–September). The average MODIS AOT within MISR AOT bins is depicted with different symbols for each year and vertical bars show the corresponding standard deviation.

each grid with a mean correlation between AOT and shortwave flux being 0.67. A minimum of 10 data points in each grid is required for F_{clr} calculation. Figure 4 shows some examples of regressions used to estimate F_{clr}. These examples were selected to show regression relationships with both high (e.g., 2001) and low (2002) correlations and differing number of data points in each grid i.e., 13 data points in 2002 as opposed to 46 in 2005. The seasonal mean F_{clr} in 5 years varies from 146 Wm^{-2} to 150 Wm^{-2} with a mean of 148 Wm^{-2} while the average F_{aero} ranges between 159 and 168 Wm^{-2} with the mean being 161 Wm^{-2}. Table 3 also shows that the DSWARF varies between −5.2 and −9.4 Wm^{-2} and the mean is −7.6 Wm^{-2}. The corresponding MISR AOT varies between 0.15 and 0.36 with 0.24 being the mean. From 7 year (1993–2002) analysis of SWARF over two stations in the Amazon, *Procopio et al.* [2004] estimated the TOA SWARF using AERONET AOT and the DISORT model. In the years 2000 through 2002, the DSWARF was reported as −5.3 to −9.9 Wm^{-2} while AOT varied between 0.55 and 1.14. Comparison with our results (Table 4) demonstrates an excellent agreement between model and observation based estimates of aerosol forcing over the Amazon.

[25] Figure 5 shows variation of TOA SWARF with variation in τ_{MISRC}. The gray symbols represent the SWARF values at each CERES pixel for respective τ_{MISRC} values during August and September in the 5 years. The insets show the frequency distribution of both SWARF and τ_{MISRC} in different bins. From Figure 5 we see that the magnitude of forcing (SWARF) is directly related to aerosol concentration (τ_{MISRC}) and the magnitude of SWARF is seen to increase with increase in τ_{MISRC}. This is as expected because higher concentration of aerosol particles in the atmosphere leads to more extinction due to backscattering and hence higher the AOT. The SWARF values at CERES pixel resolution (gray symbols) vary between 50 Wm^{-2} and −100 Wm^{-2}. However, the frequency distribution shows a small percentage of very high positive and negative forcing values. The range of SWARF indicates that smoke in the study region produced both negative and positive forcing

Table 2. Comparison of Seasonal (August–September) Mean and Standard Deviation in MODIS and MISR Aerosol Properties With AERONET Observations for 2001–2005 Over the Study Area (0°–20°S and 45°W–65°W)[a]

		AOT			AE		% FMA		% CMA	
Year	Data Points	AERO	MISR	MODIS	AERO	MISR	AERO	MISR	AERO	MISR
2000	2	0.29	0.23	0.20	1.56	1.56	70	78	30	22
2001	10	0.21 ± 0.1	0.18 ± 0.1	0.17 ± 0.1	1.57 ± 0.2	1.55 ± 0.2	63	78	37	22
2002	12	0.52 ± 0.4	0.39 ± 0.3	0.52 ± 0.4	1.77 ± 0.4	1.66 ± 0.4	63	87	37	13
2003	10	0.34 ± 0.3	0.30 ± 0.2	0.31 ± 0.3	1.46 ± 0.3	1.96 ± 0.3	65	87	35	13
2005	11	0.99 ± 0.7	0.71 ± 0.4	1.09 ± 0.8	1.73 ± 0.1	1.28 ± 0.3	78	79	22	21
Mean	45	0.47 ± 0.3	0.36 ± 0.2	0.46 ± 0.4	1.62 ± 0.1	1.60 ± 0.2	68	82	32	18

No data was found over any AERONET station area in 2004.

[a]The merged CERES-SSF and MISR L2 aerosol data from this study was collocated in space (3 × 3 CERES pixels around AERONET stations) and time (±30 min) with AERONET stations in the study area. AOT stands for aerosol optical thickness and AOT values for AERONET (AERO), MISR and MODIS are tabulated. AE denotes the angstrom exponent from both AERONET (AERO) and MISR. The second column shows the number of valid collocated data points used in calculating statistics given in table.

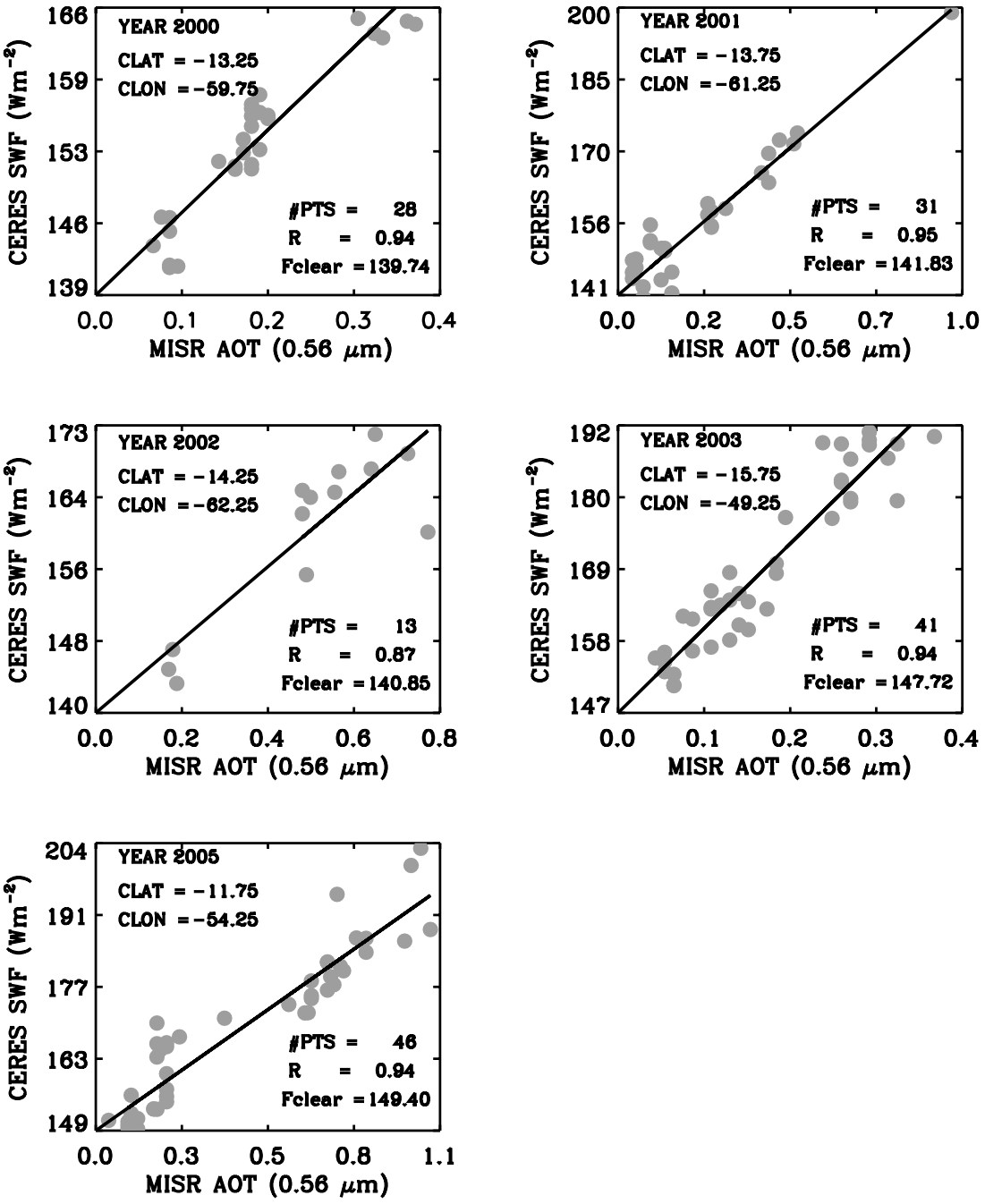

Figure 4. Examples of regressions between CERES top of atmosphere shortwave fluxes and collocated MISR AOT used to estimate F_{clr} for each year of the study period.

though the average forcing over the entire study period is negative (Table 3). Biomass burning aerosol particles are composed of nearly 50–60% organic carbon and 5–10% black carbon [*Reid et al.*, 2005]. Thus depending upon the aerosol concentration, chemical composition, and the underlying surface reflectance, smoke aerosols can both scatter and absorb solar radiation effectively [*Reid et al.*, 2005] resulting in negative and/or positive forcing. As for the surface, our study region mainly comprises of Amazon forest and savanna ecosystems in South America. The positive forcing values from each year are found to belong to the savanna ecosystem while negative forcing values come from both ecosystem types. Over highly reflective surfaces, such as the savanna, absorbing aerosols appears "darker" than the background, and can likely result in a positive TOA forcing because the downward SW flux at TOA is enhanced by aerosol absorption, as compared to the aerosol-free condition in which most SW flux is reflected back to space by the surface. For darker surfaces, such as the Amazon forest, although the aerosols are absorbing, the aerosol layer is still "brighter" than underlying surface and the TOA forcing is expected to be negative in these cases. Since, the number of pixels with positive forcing (5%–11%) is rather small in our study

Table 3. Seasonal (August–September) Mean and Standard Deviation in Quantities Estimated for 2001–2005 in the Study Region (0°–20°S and 45°W–65°W)[a]

					SWARF			
Year	Data Points	τ_{MISRC}	F_{clr}	F_{aero}	Inst	BA	DiAv	Eτ
2000	07754	0.18 ± 0.14	147.9 ± 14.1	158.9 ± 12.9	−10.9 ± 12.6	−12.7 ± 12.6	−6.1 ± 6.1	−41.97
2001	21430	0.15 ± 0.18	149.0 ± 10.6	156.7 ± 12.4	−07.7 ± 9.6	−10.9 ± 09.6	−5.2 ± 4.6	−45.59
2002	19146	0.30 ± 0.24	145.8 ± 10.6	161.6 ± 15.7	−15.8 ± 15.8	−19.7 ± 15.8	−9.4 ± 7.6	−42.77
2003	18814	0.23 ± 0.18	147.3 ± 10.0	160.3 ± 13.5	−13.0 ± 12.6	−16.3 ± 12.6	−7.8 ± 6.1	−47.49
2005	33907	0.36 ± 0.28	150.5 ± 11.3	168.2 ± 15.9	−17.7 ± 15.3	−19.5 ± 15.3	−9.3 ± 7.4	−43.01
Mean	20210	0.24 ± 0.08	148.09 ± 1.8	161.15 ± 4.4	−13.05 ± 3.9	−15.80 ± 3.9	−7.6 ± 1.9	−44.17 ± 2.3

[a]The second column shows the number of valid data points used in calculating given statistics. τ_{MISRC} is the MISR AOT within the CERES footprint. F_{clr} is the clear sky TOA shortwave flux (Wm^{-2}) and F_{aero} is the TOA shortwave flux from aerosols (Wm^{-2}). SWARF is the CERES TOA shortwave aerosol radiative forcing (Wm^{-2}). Table shows the instantaneous (Inst), Bias adjusted (BA) and diurnally averaged (DiAv) values for SWARF. The forcing efficiency for each year is denoted by $E\tau$ ($Wm^{-2}\tau^{-1}$).

(see histogram) the resultant clear sky shortwave forcing is negative (Table 3).

4.3. TOA Instantaneous Shortwave Aerosol Radiative Forcing Efficiency

[26] To determine the TOA SW aerosol radiative forcing efficiency (E_τ), we examined the regression relationship between τ_{MISRC} and the SWARF for each year (Figure 5). The slope of the regression line is E_τ. The regression line in gray is fitted to all 5 years of pixel level data (gray symbols). The black lines (in different line styles) depict the regression relationship between median SWARF values (different black symbols) and τ_{MISRC} values in 0.1 τ_{MISRC} bins for each year. Slopes estimated from such linear regression relations may be affected by outliers. To minimize these effects and to obtain stable relationships we have used median values to develop regressions. The relationship between SWARF and τ_{MISRC} is linear indicating not only the robustness of the collocation methods but also the confidence in using independent multisensor satellite data sets for quantitatively examining biomass burning SWARF. Over 5 years, the slope or the TOA E_τ in the study area varies from −42 to −47 $Wm^{-2}\ \tau^{-1}$ and the 5-year mean E_τ is −44 $Wm^{-2}\ \tau^{-1}$ (Table 3) that is also consistent with previous studies by *Li et al.* [2000] who reported values between −29 to −57 $Wm^{-2}\ \tau^{-1}$ and *Christopher et al.* [2000] who reported values between −20 to −60 $Wm^{-2}\ \tau^{-1}$ over South America (Table 4).

4.4. Qualitative Analysis of Beta Version of MISR Parameters

[27] The MISR aerosol product contains information on the spectral optical depth fraction attributable to small (SAOT) ($r < 0.35\mu m$), medium (MAOT), and ($0.35\mu m < r < 0.70\mu m$) and large (LAOT) ($r > 0.70\ \mu m$) mode aerosols. The validation of these parameters is an ongoing effort by the MISR science team and hence they are classified as beta version of the data maturity level. We use these parameters along with beta version of AE for semiquantitative analysis only, i.e., for example, size related optical depths can reveal the contribution of each aerosol size to total extinction while AE can provide insight about the type of aerosol particles because fine anthropogenic aerosols depict AE values >1 while coarse mode aerosols have values close to zero [*Eck et al.*, 1999]. Since these parameters are not yet validated, we compare MISR AE against AERONET observations and we use the spectral curvature algorithm to calculate the fine mode fraction

Table 4. Comparison of Biomass Burning Aerosol Radiative Effects and MISR Aerosol Optical Properties From This Study With Literature[a]

Reference	Region	Period	Data	AOT	TOA Instantaneous SWARF	Diurnally Averaged SWARF	Forcing Efficiency Eτ	Angstrom Exponent (AE)
Present study	Amazon	Aug–Sep, 2000–2005	Terra CERES MISR	0.24	−13.0	−7.6	−44.2	1.54
Christopher and Zhang [2002]	Amazon	Jul–Aug, 1998	GOES-8; DISTORT	0.63 ± 0.39	−45 ± 18.8	−64.6	−70	···
Li et al. [2000]	Amazon	Aug 1998	TRMM VIRS CERES	0.62–1.51	−32 to −55	···	−29 to −57	···
Christopher et al. [2000]	Brazil	Aug–Sep, 1995	SCAR-B Fu-Liou	0.6–0.8	···	···	−20 to −60	···
Procopio et al. [2004]	two locations in Amazon	Jul–Dec, 1993–1995; 1999–2002	DISORT	0.55 to 1.44	···	−5.3 to −9.9	···	···
Chand et al. [2005]	Amazon	Sept, 2002	in situ	···	···	···	···	1.4 to 2.0 $\mu = 1.8 \pm 0.1$
Reid et al. [2005]	Amazonian forest: Brazil	1993–1994 1998–1999	AERONET	0.1–3.0 $\mu = 0.74$	···	···	···	1.2–2.1
Landulfo et al. [2003]	Amazon	Sep–Oct, 2001 2002	LIDAR	0.16 0.23	···	···	···	1.6 1.8

[a]ftp://ftp.agu.org/apend/gl/2003GL018063.

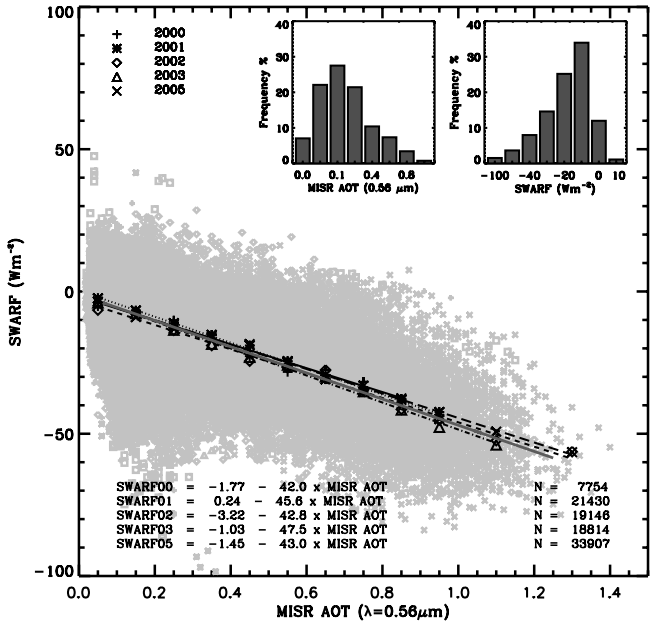

Figure 5. Relationship between collocated MISR AOT and CERES top of atmosphere shortwave aerosol radiative forcing for 2000–2005. Different symbols show AOT bin averaged values of SWARF for each year. Vertical bars represent the standard deviation of SWARF within in AOT bin.

(FMF) from spectral AERONET AOT observations in the study region [*O'Neill et al.*, 2003]. The FMF is a ratio of fine mode AOT to total AOT and fine mode in above algorithm defines aerosol particles < 0.6 μm in size [*O'Neill et al.*, 2001]. The τ_{AEROC} is multiplied by FMF to obtain the fine mode AOT (FMA) and the coarse mode AOT (CMA) is obtained by differencing τ_{AEROC} and FMA. We add the small (0.0–0.35 μm) and medium mode (0.35–0.7 μm) MISR AOTs to match the fine mode particle size definition from AERONET. The MISR-AERONET intercomparison results presented in Table 2 show a reasonable agreement between MISR and AERONET AE values while MISR shows a higher contribution of FMA(%) when compared to AERONET each year. However, both instruments show prevalence of fine particles during BB period in the study region. Also, the area mean value of AE, SAOT, MAOT, and LAOT over the study period is listed in Table 1. Comparison of these values with available literature (Table 4) also shows a good agreement. For example, *Chand et al.* [2005] report a mean AE value of 1.8 ± 0.1 while MISR reports AE of 1.58 ± 0.36. Our results give us some confidence in using MISR observations in this study while more comprehensive validations by the MISR science team are awaited.

[28] To analyze the relation of aerosol forcing with aerosol sizes we first investigate the daily trends in τ_{MISRC}, SAOT, MAOT, LAOT, and DSWARF as shown in Figure 6. Each point on a time series represents the area averaged value of these parameters on the respective day of the year. From August to September each year, the AOTs clearly show an increasing trend and DSWARF closely follows the SAOT trend. The monthly mean MODIS fire count for each year is consistent with this trend showing less burning activities in August compared to September (Figure 2). Analysis of individual years shows that the daily area average value of τ_{MISRC} can range from a low value of 0.05 in August to a high value of 0.89 in September (Figure 6c). The corresponding DSWARF is found to vary between -0.73 Wm^{-2} and -22 Wm^{-2} (Figure 6c). Also, Figure 6 clearly reveals the prevalence of small mode aerosol particles (see SAOT) during the entire study period. Table 1 shows that on an average 66% of total extinction (τ_{MISRC}) is from small sized particles (SAOT) while medium (MAOT) and large sized (LAOT) particles contribute to 16% and 18% of the $\tau_{\mathrm{MISRC.}}$ From Figure 6 we also see that SAOT appears to increase as biomass burning activity increases while MAOT and LAOT remain nearly constant. This indicates that DSWARF (which also shows an increasing trend) is largely responding to SAOT and that the biomass burning aerosol particles in the study region are primarily responsible for the aerosol radiative forcing in this season.

[29] Figure 6a through Figure 6e shows an increase in τ_{MISRC} and SAOT from the year 2000 to 2005 except for 2003 wherein daily mean τ_{MISRC} values are higher than 2000 and 2001 but lower than 2002. Also, in 2003 MAOT (SAOT) is dominant (small) in August while SAOT (MAOT) dominates (small) in September resulting in equal contribution from SAOT and MAOT during the season (see Table 1). From the 2003 MODIS fire data we find that the number of fires in August of 2003 was less than the August fire activity in all other years (see Figure 2). Lower BB activity in August possibly explains why 2003 is in disagreement with other years in terms of SAOT and MAOT apportionment.

[30] Figure 7 depicts the interannual variation in the seasonal mean τ_{MISRC} and DSWARF (max height of the bars) among small (blue), medium (green) and large (red) mode aerosol particles during 5 years. Figure 7 also shows that the total extinction is dominated by small aerosol particles (blue) during the entire study period. MISR derived AE values (Tables 1 and 2) are also in agreement with this (AE > 1.3). These results agree with *Reid et al.* [2005]

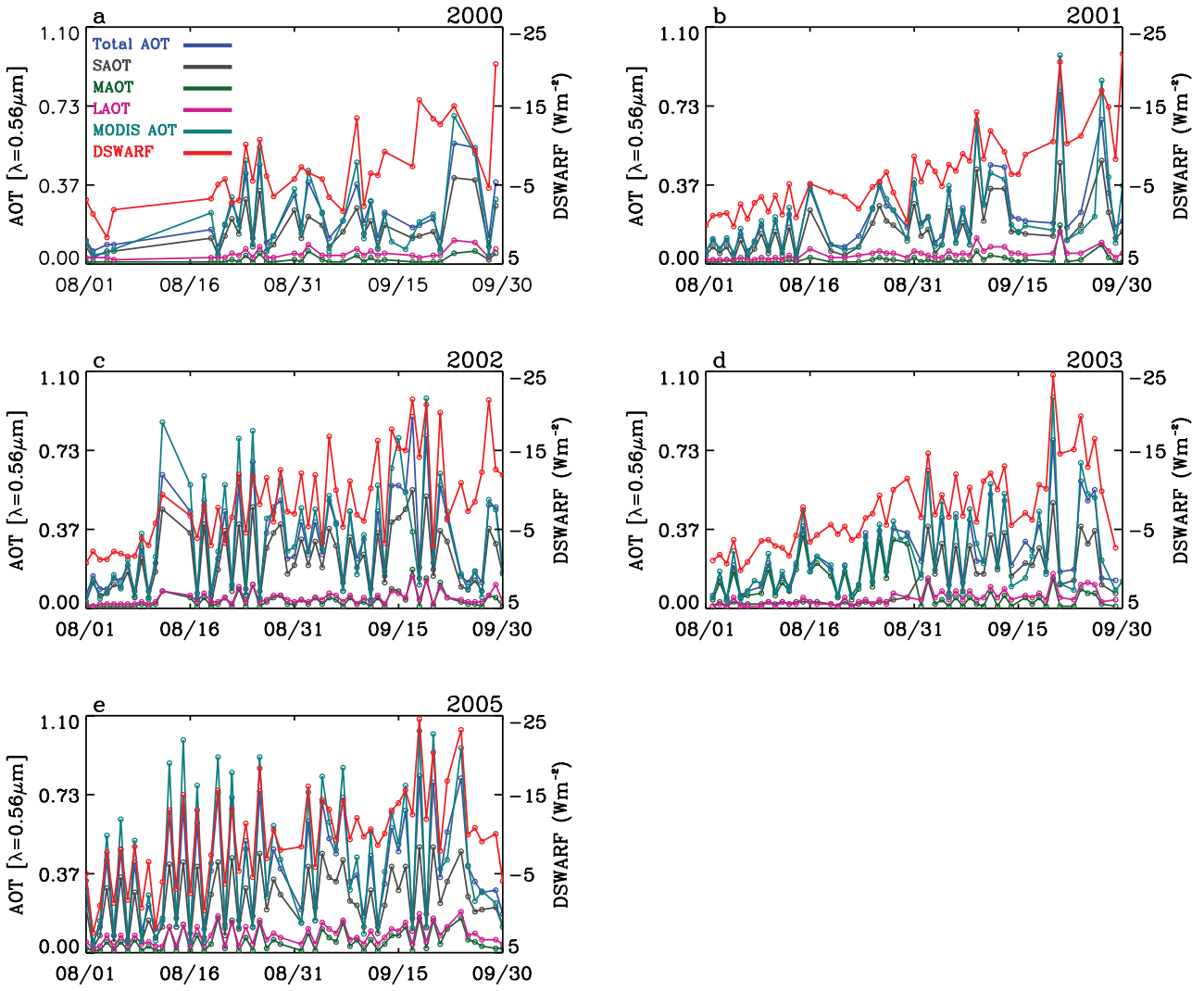

Figure 6. Daily variation of total, small, medium, and large mode MISR aerosol optical thickness (AOT), MODIS AOT, and TOA diurnally averaged SWARF. Each point in the time series represents the 5-year area average value. The AOT values are depicted on primary (left) *y* axis while the secondary (right) *y* axis denotes diurnally averaged SWARF values.

who note that combustion from BB results in 80–90% accumulation/small mode (d < 1 μm) aerosol particles that are primarily produced from condensation processes [*Reid et al.*, 1998]. This is the first time that a satellite based study shows the prevalence of small aerosol particles in BB periods for multiple years and the excellent agreement with literature/ground based observations (Tables 2 and 4) further strengthens the confidence in using these multisensor data for aerosol forcing studies.

5. Uncertainty in Forcing Calculation

[31] Finally we make an attempt to estimate the uncertainty in our calculation of SWARF. Table 5 lists the primary sources of uncertainties associated with satellite based assessment of SWARF. Estimating uncertainty from observation based methods is challenging because it is often difficult to quantify some of the uncertainties such as in the ADMs used to convert radiance to flux. On the other hand, modeling based studies use ensemble of experiments to estimate the uncertainties [*Bellouin et al.*, 2005; *Schulz et al.*, 2006]. We use uncertainty in calibrated CERES radiance, unfiltering of CERES SW radiance and radiance-to-flux conversion from literature (see Table 5). We estimate the uncertainty in F_{clr} by accounting for the uncertainty in MISR AOT as the F_{clr} has been estimated by regressing TOA CERES SWF against MISR AOT (Figure 4). The mean aerosol forcing efficiency ($E\tau$) is ~44.2 $Wm^{-2}\tau^{-1}$. Therefore maximum uncertainty of ±0.05 in MISR AOT would translate to 2.2 Wm^{-2} (or ±1.1 Wm^{-2}) uncertainty in clear sky flux (F_{clr}). The uncertainty due to subpixel cloud contamination is obtained by relaxing the percentage cloud cover by 1%, 5% and 10%. This changes DSWARF by ~0.5 Wm^{-2}. The uncertainty in CERES-Terra clear sky SW ADM's over land is <0.5% [*Loeb et al.*, 2007]. The clear sky SW ADM uncertainty over land is then ±0.4 Wm^{-2} (0.5% of mean F_{clr}). Assuming that all the uncertainties (Table 5) are uncorrelated we estimate that the total uncertainty in DSWARF to be $(0.4^2 + 0.4^2 + 0.4^2 + 1.1^2 + 0.5^2)^{1/2}$ =

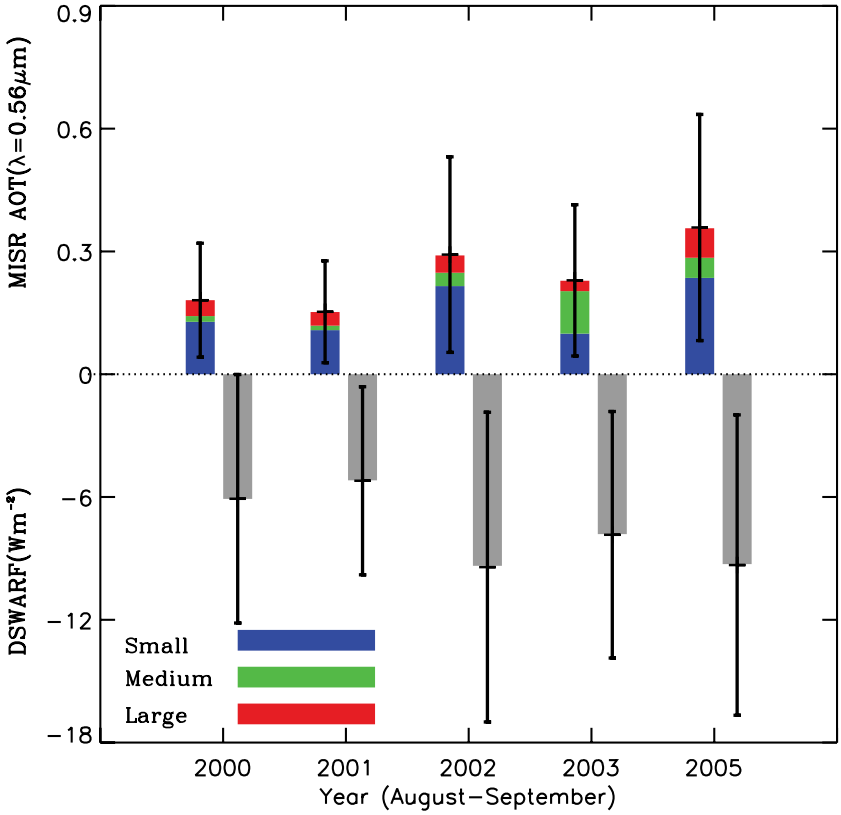

Figure 7. Area-averaged MISR aerosol optical thickness in three particle size bins: small ($r < 0.35$ μm), medium (0.35 μm $< r < 0.70$ μm) and large ($r > 0.70$ μm), during August–September for 2000–2005. Also indicated is the corresponding CERES top of atmosphere diurnally averaged shortwave forcing values. Vertical bars show the standard deviations.

1.4 Wm^{-2}. As AOT retrievals mature coupled with development of angular models we anticipate that these uncertainties can be reduced.

6. Summary and Conclusions

[32] Five years (2000–2005, excluding 2004) of multispectral, multiangle, and broadband satellite observations over the Amazon region were analyzed to estimate the cloud free TOA direct shortwave aerosol radiative forcing during the peak biomass burning season of August and September. The MODIS data in SSF product was used to eliminate clouds in the CERES footprint. MISR aerosol data sets were collocated within the CERES footprint and were used to identify aerosol particles. Corresponding TOA CERES shortwave fluxes were used to estimate clear sky and aerosol fluxes. The difference between clear sky and aerosol fluxes is reported as TOA SWARF. We account for sample biases and diurnal variation using previously established methods and report AOT collocated within CERES footprint from MISR and MODIS along with the CERES SWARF for five years.

[33] A high linear correlation is found between MODIS and MISR AOT within the CERES footprint with MODIS AOT being consistently higher than MISR AOT. Over the 5 years of study the mean MISR AOT increased from 0.17 to 0.36 while TOA SWARF increased from -5.2 Wm^{-2} to -9.3 Wm^{-2}. The 5-year mean MISR AOT and SWARF are 0.24 and -7.6 Wm^{-2} respectively. These values are consistent with other studies that used AERONET AOT and radiative transfer calculations from point locations [e.g., *Procopio et al.*, 2004]. The mean aerosol radiative forcing efficiency at the TOA over 5 years is -44.2 Wm^{-2} τ^{-1} and can serve as a constraint in numerical modeling studies' attempt to model the impact of biomass burning aerosols on the TOA radiation.

Table 5. Sources of Uncertainty in Satellite Based Estimation of Diurnally Averaged SWARF and the Associated Magnitudes of Uncertainty

	Source of Uncertainty	Uncertainty	Reference
1.	calibration of CERES radiances	~0.4 Wm^{-2}	*Priestley et al.* [2000]
2.	conversion of filtered SW radiances to unfiltered SW radiances	~0.4 Wm^{-2}	*Loeb et al.* [2001]
3.	CERES radiance to flux conversion over land	~0.4 Wm^{-2}	*Loeb et al.* [2007]
4.	estimation of clear sky flux (F_{clr})	~1.1 Wm^{-2}	present study
5.	subpixel cloud contamination	~0.5 Wm^{-2}	present study
	combined uncertainty	*1.39 Wm^{-2}*	Present Study

Total Uncertainty = $[(0.4)^2_+ (0.4)^2_+(0.4)^2_+(1.1)^2_+(0.5)^2]^{1/2} = 1.39$.

[34] Current sensors such as the MISR are beginning to retrieve aerosol properties such as fractionated AOT in three particle size bins (small, medium, and large). Although these properties are yet to be fully validated and are deemed ''beta quality'' we assessed AE and fractionated AOT as a function of SWARF. Our analysis indicates that the 5-year mean MISR AE of 1.54 is consistent with those reported previously in the literature (Table 4). Aerosol optical properties from MISR also agree reasonably with AERONET in this study (Table 2). Distribution of AOT as a function of aerosol sizes shows that 66 % of aerosols are in the small, 16% are in the medium and 18% are in the large size category that also appears to be consistent with previous studies. Investigation of daily variation of AOT and DSWARF shows a one-to-one relation with values being lower in August and increasing by September in accordance with increasing burning activities from August to September.

[35] Finally, we estimate the uncertainty in the DSWARF estimates stemming from bias correction, diurnal averaging, F_{clr} computation, cloud contamination, CERES radiance unfiltering and radiance-to-flux conversion. A total uncertainty of 1.4 Wm^{-2} is found to be associated with our DSWARF estimates which translate to uncertainty of 18%. This study clearly reveals that multisensor approaches continue to enhance our understanding of the role of aerosol particles on the climate system. The methods developed in this paper could be used to assess aerosol radiative effects over global land areas.

[36] **Acknowledgments.** This research was supported by NASA's Radiation Sciences, Interdisciplinary Sciences, EOS, and ACMAP programs. Pawan Gupta was supported by NASA Headquarters under the Earth and Space Science Fellowship (NESSF) grant. The CERES data were obtained from the NASA Langley Research Center Atmospheric Sciences Data Center, the MODIS data were obtained through the Goddard Space Flight Center Data Center. We thank the (Project/PI) for (its/theirs) effort in establishing and maintaining AERONET sites used in our investigation. We thank Ralph A. Kahn and Norman G. Loeb for their valuable discussion during the research.

References

Abdou, W. A., et al. (2005), Comparison of coincident multiangle imaging spectroradiometer and moderate resolution imaging spectroradiometer aerosol optical depths over land and ocean scenes containing aerosol robotic network sites, *J. Geophys. Res.*, *110*, D10S07, doi:10.1029/2004JD004693.

Andreae, M. (1991), Biomass burning: Its history, use and distribution and its impact on environmental quality and global climate. *Global Biomass Burning: Atmospheric, Climatic and Biospheric Implications*, pp. 3–21, MIT Press, Cambridge, Mass.

Bellouin, N., O. Boucher, J. Haywood, and R. M. Shekar (2005), Global estimate of aerosol direct radiative forcing from satellite measurements, *Nature*, *438*(7071), 1138–1141.

Chand, D., et al. (2005), Optical and physical properties of aerosols in the boundary layer and free troposphere over the Amazon Basin during the biomass burning season, *Atmos. Chem. Phys. Disc.*, *5*, 4373–4406.

Christopher, S. A., X. Li, R. M. Welch, P. V. Hobbs, J. S. Reid, and T. F. Eck (2000), Estimation of downward and top-of-atmosphere shortwave irradiances in biomass burning regions during SCAR-B, *J. Appl. Meteorol.*, *39*, 1742–1753.

Christopher, S. A., and J. Zhang (2002), Daytime variation of shortwave direct radiative forcing of biomass burning aerosols from GOES 8 imager, *J. Atmos. Sci.*, *59*(2), 681–691.

Christopher, S. A., and J. Zhang (2004), Cloud-free shortwave aerosol radiative effect over oceans: Strategies for identifying anthropogenic forcing from Terra satellite measurements, *Geophys. Res. Lett.*, *31*, L18101, doi:10.1029/2004GL020510.

Christopher, S. A., J. Zhang, Y. J. Kaufman, and L. A. Remer (2006), Satellite-based assessment of top of atmosphere anthropogenic aerosol radiative forcing over cloud-free oceans, *Geophys. Res. Lett.*, *33*, L15816, doi:10.1029/2005GL025535.

Dubovik, O., and M. D. King (2000), A flexible inversion algorithm for retrieval of aerosol optical properties from Sun and sky radiance measurements, *J. Geophys. Res.*, *105*(D16), 20,673–20,696.

Eck, T. F., B. N. Holben, J. S. Reid, O. Dubovik, A. Smirnov, N. T. O'Neill, I. Slutsker, and S. Kinne (1999), Wavelength dependence of the optical depth of biomass burning, urban, and desert dust aerosols, *J. Geophys. Res.*, *104*(D24), 31,333–31,349.

Giglio, L., J. Descloitres, C. O. Justice, and Y. Kaufman (2003), An enhanced contextual fire detection algorithm for MODIS, *Remote Sens. Environ.*, *87*, 273–282.

Gupta, P., F. Patadia, and S. A. Christopher (2008), Multi-sensor data product fusion for aerosol research, *IEEE Trans. Geosci. Remote Sens.*, TGRS-2007-00313, in press.

Hao, W. M., and M. H. Liu (1994), Spatial and temporal distribution of biomass burning, *Global Biogeochem. Cycles*, *8*, 495–503.

Holben, B., et al. (1998), AERONET: A federated instrument network and data archive for aerosol characterization, *Remote Sens. Environ.*, *66*, 1–16.

Holben, B. N., et al. (2001), An emerging ground-based aerosol climatology: Aerosol optical depth from AERONET, *J. Geophys. Res.*, *106*(D11), 12,067–12,097.

Jones, T. A., and S. A. Christopher (2007), Is the top of atmosphere dust net radiative effect different between Terra and Aqua?, *Geophys. Res. Lett.*, *34*, L02812, doi:10.1029/2006GL028262.

Justice, C. O., L. Giglio, S. Korontzi, J. Owens, J. T. Morisette, D. Roy, J. Descloitres, S. Alleaume, F. Petitcolin, and Y. Kaufman (2002), The MODIS fire products, *Remote Sens. Environ.*, *83*, 244–262.

Kahn, R., B. Gaitley, J. Martonchik, D. Diner, K. Crean, and B. Holben (2005), Multiangle imaging spectroradiometer (MISR) global aerosol optical depth validation based on two years of coincident AERONET observations, *J. Geophys. Res.*, *110*, D10S04, doi:10.1029/2004JD004706.

Kaufman, Y. J., D. Tanre, and O. Boucher (2002), A satellite view of aerosols in the climate system, *Nature*, *419*, 215–223.

Koren, I., L. A. Remer, and K. M. Longo (2007), Reversal of trend of biomass burning in the Amazon, *Geophys. Res. Lett.*, *34*, L20404, doi:10.1029/2007GL031530.

Landulfo, E., A. P. Papayannis, A. D. A. Artaxo, A. Z. Castanho, R. F. De Freitas, N. D. Souza, M. P. Vieira Junior, O. R. Jorge, V. Sanchez-Ccoyllo, and D. S. Moreira (2003), Synergetic measurements of aerosol over Sao Paulo, Brazil, using LIDAR, sunphotometer and satellite data during the dry season, *Atmos. Chem. Phys.*, *3*, 1523–1539.

Levy, R. C., L. A. Remer, S. Mattoo, E. Vermote, and Y. J. Kaufman (2007), Second generation operational algorithm: Retrieving aerosol properties over land from MODIS spectral reflectance, *J. Geophys. Res.*, *112*, D13211, doi:10.1029/2006JD007811.

Li, X., S. A. Christopher, J. Chou, and R. M. Welch (2000), Estimation of shortwave direct radiative forcing of biomass burning aerosols using angular dependence models, *J. Appl. Meteorol.*, *39*, 2278–2291.

Li, F., A. M. Vogelmann, and V. Ramanathan (2004), Saharan dust aerosol radiative forcing measured from space, *J. Clim.*, *17*, 2558–2571.

Loeb, N. G., and S. Kato (2002), Top-of-atmosphere direct radiative effect of aerosols over the tropical oceans from the Clouds and the Earth's Radiant Energy System (CERES) satellite instrument, *J. Clim.*, *15*, 1474–1484.

Loeb, N. G., N. Manalo-Smith, S. Kato, W. F. Miller, S. K. Gupta, P. Minnis, and B. A. Wielicki (2003a), Angular distribution models for top-of-atmosphere radiative flux estimation from the clouds and the Earth's radiant energy system instrument on the tropical rainfall measuring mission satellite. Part I: Methodology, *J. Appl. Meteorol.*, *42*, 240–265.

Loeb, N. G., K. Loukachine, N. Manalo-Smith, B. A. Wielicki, and D. F. Young (2003b), Angular distribution models for top-of-atmosphere radiative flux estimation from the clouds and the Earth's radiant energy system instrument on the tropical rainfall measuring mission satellite. Part II: Validation, *J. Appl. Meteorol.*, *42*, 1748–1769.

Loeb, N. G., S. Kato, K. Loukachine, and N. Manalo-Smith (2005), Angular distribution models for top-of-atmosphere radiative flux estimation from the clouds and the Earth's radiant energy system instrument on the *Terra* satellite. Part I: Methodology, *J. Atmos. Oceanic Technol.*, *22*, 338–351.

Loeb, N. G., S. Kato, K. Loukachine, N. Manalo-Smith, and D. R. Doelling (2007), Angular distribution models for top-of-atmosphere radiative flux estimation from the clouds and the Earth's radiant energy system instrument on the *Terra* satellite, *J. Atmos. Oceanic Technol.*, *24*, 564–584.

Martins, J. V., D. Tanré, L. Remer, Y. Kaufman, S. Mattoo, and R. Levy (2002), MODIS cloud screening for remote sensing of aerosols over oceans using spatial variability, *Geophys. Res. Lett.*, *29*(12), 8009, doi:10.1029/2001GL013252.

Martonchik, J. V., D. J. Diner, R. A. Kahn, T. P. Ackerman, M. M. Verstraete, P. Bernard, and H. R. Gordon (1998), Techniques for the retrieval of aerosol properties over land and ocean using multiangle imaging, *IEEE Trans. Geosci. Remote Sens.*, *36*, 1212–1227.

Martonchik, J. V., D. J. Diner, K. A. Crean, and M. A. Bull (2002), Regional aerosol retrieval results from MISR, *IEEE Trans. Geosci. Remote Sens.*, *40*, 1520–1531.

Minnis, P., D. F. Young, S. Sun-Mack, P. W. Heck, D. R. Doelling, and Q. Trepte (2003), CERES cloud property retrievals from imagers on TRMM, Terra, and Aqua, *Proc. SPIE 10th International Symposium on Remote Sensing: Conference on Remote Sensing of Clouds and the Atmosphere VII*, SPIE, Barcelona, 8–12 Sept., 37–48.

Morisette, J. T., L. Giglio, I. Csiszar, A. Setzer, W. Schroeder, D. Morton, and C. O. Justice (2005), Validation of MODIS active fire detection products derived from two algorithms, *Earth Interact.*, *9*(9), 1–25.

O'Neill, N. T., T. F. Eck, A. Smirnov, B. N. Holben, and S. Thulasiraman (2003), Spectral discrimination of coarse and fine mode optical depth, *J. Geophys. Res.*, *108*(D17), 4559, doi:10.1029/2002JD002975.

O'Neill, N. T., T. F. Eck, B. N. Holben, A. Smirnov, O. Dubovik, and A. Royer (2001), Bimodal size distribution influences on the variation of Angstrom derivatives in spectral and optical depth space, *J. Geophys. Res.*, *106*(D9), 9787–9806.

Prins, E. M., J. M. Feltz, W. P. Menzel, and D. E. Ward (1998), An overview of GOES-8 diurnal fire and smoke results for SCAR-B and 1995 fire season in South America, *J. Geophys. Res.*, *103*(D24), 31,821–31,835.

Procopio, A. S., P. Artaxo, Y. J. Kaufman, L. A. Remer, J. S. Schafer, and B. N. Holben (2004), Multiyear analysis of Amazonian biomass burning smoke radiative forcing of climate, *Geophys. Res. Lett.*, *31*, L03108, doi:10.1029/2003GL018646.

Reid, J. S., P. V. Hobbs, R. J. Ferek, D. R. Blake, J. V. Martins, M. R. Dunlap, and C. Liousse (1998), Physical, chemical and optical properties of regional hazes dominated by smoke in Brazil, *J. Geophys. Res.*, *103*(D24), 32,059–32,080.

Reid, J. S., R. Koppmann, T. F. Eck, and D. P. Eleuterio (2005), A review of biomass burning emissions. part II: Intensive physical properties of biomass burning particles, *Atmos. Chem. Phys. Disc.*, *5*, 5201–5260.

Remer, L. A., and Y. J. Kaufman (2005), Aerosol effect on the distribution of solar radiation over the clear-sky global oceans derived from four years of MODIS retrievals, *Atmos. Chem. Phys. Disc.*, *5*, 5007–5038.

Remer, L. A., et al. (2005), The MODIS aerosol algorithm, products and validation, *J. Atmos. Sci.*, *62*, 947–973.

Schulz, M., et al. (2006), Radiative forcing by aerosols as derived from the AeroCom present-day and pre-industrial simulations, *Atmos. Chem. Phys.*, *6*, 5225–5246.

Smith, G. L. (1994), Effects of time response on the point spread function of a scanning radiometer, *Appl. Opt.*, *33*, 7031–7037.

Stott, P. A., and J. A. Kettleborough (2002), Origins and estimates of uncertainty in predictions of twenty-first century temperature rise, *Nature*, *416*, 723–726.

Stott, P. A., et al. (2006), Observational constraints on past attributable warming and predictions of future global warming, *J. Clim.*, *19*, 3055–3069.

Wielicki, B. A., B. R. Barkstrom, E. F. Harrison, R. B. Lee, G. Louis Smith, and J. E. Cooper (1996), Clouds and the Earth's Radiant Energy System (CERES): An Earth observing system experiment, *Bull. Am. Meteorol. Soc.*, *77*, 853–868.

Zhang, J., and S. A. Christopher (2003), Longwave radiative forcing of dust aerosols over Saharan Desert estimated from MODIS, MISR, and CERES observations from Terra, *Geophys. Res. Lett.*, *30*(23), 2188, doi:10.1029/2003GL018479.

Zhang, J., S. A. Christopher, L. A. Remer, and Y. J. Kaufman (2005), Shortwave aerosol radiative forcing over cloud-free oceans from Terra: 2. Seasonal and global distributions, *J. Geophys. Res.*, *110*, D10S24, doi:10.1029/2004JD005009.

S. A. Christopher, P. Gupta, and F. Patadia, Department of Atmospheric Science, The University of Alabama in Huntsville, 320 Sparkman Drive, Huntsville, AL 35806, USA. (sundar@nsstc.uah.edu)

J. S. Reid, Aerosol and Radiation Section, Marine Meteorology Division, Naval Research Laboratory, Monterey, CA, USA.